INSTITUTE OF PHYSICS PUBLISHING JOURNAL OF PHYSICS: CONDENSED MATTER

J. Phys.: Condens. Matter **13** (2001) 8287–8301 PII: S0953-8984(01)21717-2

Neutron scattering studies of disordered carbon anode materials

P Papanek[1,2], W A Kamitakahara[2], P Zhou[3] and J E Fischer[3]

[1] Department of Materials Science and Engineering, University of Pennsylvania, Philadelphia, PA 19104, USA
[2] NIST Center for Neutron Research, National Institute of Standards and Technology, Gaithersburg, MD 20899, USA
[3] Department of Materials Science and Engineering and Laboratory for Research on the Structure of Matter, University of Pennsylvania, Philadelphia, PA 19104, USA

Received 7 February 2001
Published 23 August 2001
Online at stacks.iop.org/JPhysCM/13/8287

Abstract

Carbon-based anodes show many promising properties in lithium-ion rechargeable batteries. So-called 'disordered carbons' are characterized by a substantial amount of residual hydrogen, and exhibit large Li uptake capacities. We have employed a variety of neutron scattering techniques, coupled with computer simulations, to study the composition, local atomic structure, and vibrational dynamics of such materials. Radial distribution function analysis of neutron diffraction data, and incoherent inelastic scattering show that the structural motif is a planar graphene fragment, with edge carbons terminated by single hydrogen atoms, and random stacking between fragments. The vibrational spectra of the hydrogen-rich carbons are remarkably similar to the spectra of the polycyclic aromatic hydrocarbon coronene in the medium-frequency region. At low frequencies, only a boson peak is observed, characteristic for glassy and disordered materials, and this feature shifts upon doping. The results are consistent with two proposed mechanisms for Li capacity, one analogous to conventional intercalation but with Li on both sides of graphene fragments, the other involving bonding of Li to H-terminated edge carbons.

1. Introduction

Considerable progress has been made in the development of rechargeable lithium batteries in recent years. Early problems with safety and limited cycle life were solved by replacing Li-metal anodes with lithium intercalation compounds, such as $LiWO_2$ or LiC_6 (lithium-intercalated graphite), for which the chemical potential of the intercalated Li is close to that of Li metal. Layered materials, for example $LiNiO_2$ or $LiCoO_2$, which have potentials of about 4 V against Li, are used as the cathodes. Lithium ions then shuttle back and forth through an

electrolyte to intercalate into either the cathode or the anode hosts, as the battery is discharged or charged, respectively.

Carbon-based anodes show the most promising properties in lithium-ion batteries. Current industrial production, exceeding 15 million batteries per month, is dominated by highly graphitic carbons. However, various other kinds of material have been studied, and disordered carbons, in particular, offer some attractive features such as higher Li capacity and/or longer cycle life (here, the term 'disordered' is used to make a distinction from 'amorphous' carbon which usually refers to sp^3-bonded hard carbons). In order to maximize the stored energy per unit mass in a battery, it is important to determine which types of carbon react reversibly with the largest amount of lithium. Carbons prepared by pyrolysing soft-carbon precursors at temperatures above 2400 °C are well graphitized and show Li uptake capacity corresponding to ∼350 mA h g^{-1} of carbon (for comparison, crystalline LiC_6 shows a capacity corresponding to 372 mA h g^{-1}). On the other hand, materials obtained by pyrolysing organic solids in an inert gas at temperatures $T \leqslant 700$ °C exhibit surprisingly large capacities, reaching almost 900 mA h g^{-1}. It was realized that carbons prepared in this way contain substantial residual hydrogen, and an empirical correlation between Li capacity and the amount of hydrogen was found, suggesting a limiting value of one 'excess' Li per H [1].

The graphite-intercalated compound LiC_6 has been studied extensively and thus offers some clues for understanding Li behaviour in disordered carbons. The lithium ions in LiC_6 are centred on high-symmetry interstitial sites located between eclipsed hexagons on adjacent graphite layers (Li–C coordination: 12). Only one third of the available sites are occupied, corresponding to second-nearest hexagon neighbours, and an ordered $\sqrt{3} \times \sqrt{3}$ in-plane superlattice is formed. Local commensurability is the consequence of strong Li–C interactions, and the occupancy of second-neighbour sites within a gallery results from intralayer Li–Li repulsion. Strong interactions between lithium and carbon layers also result in the characteristic $A\alpha A\alpha$ stacking (A = graphite layer, α = Li layer) [2].

To explain the high Li capacity of disordered carbons, several hypotheses have been proposed. In the 'house-of-cards' model, the host carbon structure is pictured as randomly stacked single-layer graphene fragments, such that both sides of the graphene sheet are accessible to lithium, resulting in a maximum Li capacity twice that of LiC_6. This model may be relevant to carbons with relatively low hydrogen content (pyrolysis temperatures $\geqslant$1000 °C). Substantial porosity on a length scale comparable to the graphene fragment size is necessary in order to minimize Coulomb repulsion between Li ions on neighbouring 'doped' fragments. Another model, specific to low-T pyrolysed materials with large H/C content, suggests the existence of Li_2 covalent molecules in the carbon material. Sato *et al* [3] synthesized a disordered carbon sample by a heat treatment of poly(*p*-phenylene) under hydrogen flow at 700 °C with a resulting H/C ratio of 0.24. X-ray diffraction of this disordered carbon showed no clear (002) reflections, and the measured Li uptake capacity, 680 mA h g^{-1}, significantly exceeded that of the first-stage LiC_6 stoichiometry. Analysis of the ^{7}Li NMR of Li-doped carbon revealed a Lorentzian line positioned at −0.62 ppm, which was attributed to molecular Li_2. The suggested model assumes the coexistence of ionic Li in the second-nearest-neighbour interstitial sites and covalently bonded Li_2 molecules positioned epitaxially over first-neighbour hexagons, such that lithium is located above each hexagon, corresponding to the stoichiometry LiC_2. We note that intercalated graphite LiC_2 can in fact be obtained by high-pressure synthesis [4], but upon releasing the pressure the structure immediately decomposes. Hence, nearest-neighbour occupancy seems very unlikely at ambient pressure.

On the basis of the results of quantum chemical simulations, a different mechanism has been proposed to explain the large capacity of hydrogen-rich carbons [5]. These calculations predict that in parallel with the usual lithium intercalation (interstitial Li centred over a carbon

ring), Li also binds covalently to hydrogen-terminated edges of a graphene fragment. This second mechanism can be explained using as an example the interactions between lithium and a small aromatic hydrocarbon, pyrene $C_{16}H_{10}$. Figure 1(a) shows the optimized structure (local energy minimum) of pyrene and two lithium atoms, introduced above and below the molecular plane, near the carbon ring terminated by three H atoms. The relaxed geometry maintains the interstitial Li positions with about 2 Å distance between Li and the molecular plane (∼8% greater than the experimental value for LiC_6 [2]). On the other hand, if the initial lithium position is near the carbon ring terminated by two hexagons, the Li atoms move off the interstitial sites and form polar covalent bonds with the two peripheral carbons, as shown in figure 1(b). This requires sp^3 hybridization of both carbons such that the conjugation of that particular ring is destroyed. The sp^3 character is also confirmed by the greatly increased bond length, 1.52 Å, between the two carbons [5]. Larger polycyclic aromatic hydrocarbons (PAH) also show similar behaviour. Coronene, $C_{24}H_{12}$, readily forms six C–Li bonds along its perimeter (figure 2), and similar effects were later obtained in simulations for even larger PAH molecules [6].

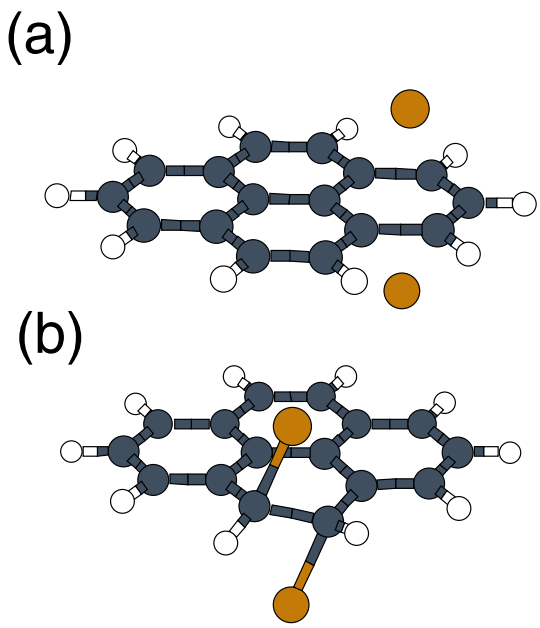

Figure 1. Optimized structures (local energy minima) for the pyrene + 2 Li system. (a) Lithium atoms remain above and below the ring centre, in positions corresponding to interstitial sites in lithium–graphite. (b) Li atoms move off the interstitial sites and form polar covalent bonds with the two peripheral carbons, which show evidence of sp^3 hybridization.

Since the binding energy per Li is not too different from that of the interstitial intercalation reaction, the two processes may occur at similar potentials during electrochemical cycling, and thus both will contribute to the reversible capacity of the carbon anode. However, the bonding mechanism will be operative only if the edge carbon atoms are each saturated with a single hydrogen, since then an extra electron is available for bonding. Two edge hydrogens would result in a chemically inert methylene moiety.

In this work, we present the results of experimental measurements of composition, local atomic structure, and vibrational dynamics (addressing the local hydrogen arrangement) in several disordered carbon samples. Various neutron scattering techniques, such as prompt-

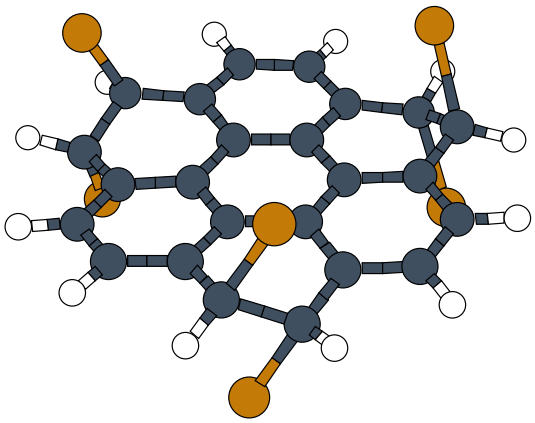

Figure 2. The stable configuration of six Li bonded to coronene, $C_{24}H_{12}$. The lithium atoms are bonded to alternating peripheral rings even in cases where they are initially introduced above and below the central hexagon.

gamma activation analysis, radial distribution function analysis of neutron scattering data, and the inelastic incoherent neutron scattering technique, were employed.

2. Experimental procedure

2.1. Composition and local structure

The disordered carbon samples, used in our experiments, were synthesized by pyrolysing the epoxy Novolac resin poly[(phenyl glycidyl ether)-co-formaldehyde] at different temperatures in an inert atmosphere. In the following, the disordered carbon synthesized at 650 °C is denoted as DC650, and the sample synthesized at 1000 °C is denoted as DC1000. We have also studied a sample from a commercial by-product of coal-tar-pitch processing, denoted as NT10.

To determine the atomic composition, standard analytical methods (e.g., combustion) and prompt-gamma activation analysis (PGAA) were used. The latter was performed using the PGAA instrument at the NIST Center for Neutron Research. The PGAA method is based on the fact that many nuclei, excited upon capturing a slow neutron, emit characteristic gamma rays. For example, a hydrogen atom captures a neutron to form an excited state of deuterium which decays rapidly by emission of a 2223.23 keV gamma ray. The PGAA technique has good sensitivity to hydrogen, for which the detection limit is $\sim$3 μg in a gram of material. The measured H/C atomic ratios in the samples DC650, DC1000, and NT10 were 0.24 ± 0.01, 0.04 ± 0.01, and 0.38 ± 0.01, respectively.

The samples were also Li doped electrochemically, using a Li-metal electrode and non-aqueous electrolytes. However, in this procedure we could not avoid the growth of a solid-electrolyte interphase (SEI) on the surface of the carbon electrodes due to partial decomposition of the electrolyte. The best results, with small changes in the H/C composition and a substantial Li uptake, were obtained for the DC650 carbon. The final Li/C doping concentration was determined as 0.32 ± 0.01 from PGAA and electrochemical data.

X-ray diffraction profiles of the disordered carbon samples display weak, broad maxima. In general, such diffraction patterns are often interpreted as if the materials were perfectly crystalline, and interlayer distances and crystallite sizes are deduced from peak positions and linewidths. Although useful for classifying different materials, this procedure cannot be justified quantitatively. In disordered materials, the diffraction maxima do not occur at the Bragg positions (especially in layer materials [7]) and the linewidths include other contributions beside finite-size effects (e.g., paracrystallinity). However, physical quantities

characterizing the local structure, such as interatomic distances, average bond angles, and coordination numbers, are still well defined for amorphous or disordered materials, and can be studied using the pair distribution function or radial distribution function (RDF) analysis. The RDF method was used in recent studies of nanoporous carbons [8], and amorphous carbons prepared by argon plasma sputtering [9].

In an RDF analysis, the differential correlation function $D(r)$ is derived by Fourier transforming the experimentally determined elastic structure factor $S(Q)$:

$$D(r) = \frac{2}{\pi}\int_0^\infty Q[S(Q) - 1]\sin(Qr)\,\mathrm{d}Q = 4\pi r[\rho(r) - \rho_0] \tag{1}$$

where Q is the momentum transfer, $\rho(r)$ is the number of atoms per unit volume at r, and ρ_0 is the average density. The RDF is then defined as $4\pi r^2\rho(r)$. In practice, the integral is truncated at some maximum $Q_{\max}$ limiting the spatial resolution. Hence, it is important to collect the scattering data with instruments where high $Q_{\max}$ can be achieved. We used the Glass–Liquid–Amorphous material Diffractometer (GLAD) at the Intense Pulsed Neutron Source in Argonne National Laboratory, with $Q_{\max} \geqslant 30$ Å^{-1}. Details about the GLAD instrument are given elsewhere [10].

The differential correlation functions $D(r)$ of the disordered carbons DC650 and DC1000, derived from neutron scattering data, are shown in figure 3. For comparison, the experimental $D(r)$ of graphite is also plotted (solid line, offset vertically for clarity). The Fourier integral was truncated at 25 Å^{-1}, a compromise between minimizing the truncation broadening and eliminating spurious features from the noise in $S(Q)$ at high Q. The correlation functions of the two disordered carbons are quite similar, and most peaks occur at the same positions as in graphite. This indicates the same average bond length and angle, i.e., a hexagonal planar local motif and sp^2-hybridized carbon network.

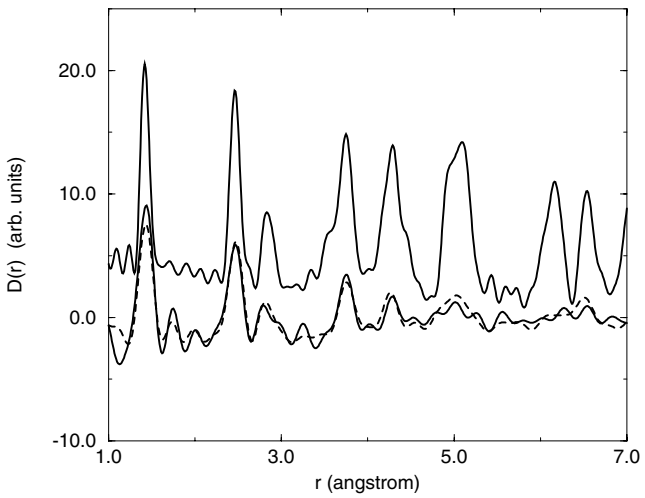

Figure 3. Differential correlation functions of the disordered carbons DC650 (solid line) and DC1000 (dashed line). The upper solid line represents $D(r)$ for graphite, with the origin shifted vertically for clarity.

For both disordered carbons, the peak intensities are weaker than in graphite, and their amplitudes diminish further with increasing r. The smaller intensities for low-order peaks imply finite-size graphene fragments, such that there are a significant number of edge C atoms having only two neighbours. The absence of strong peaks above ∼6 Å suggests the approx-

imate in-plane size, and the absence of the shoulder at 3.35 Å (visible in graphite) signifies the loss of AB stacking in the disordered carbons.

Model calculations, comparing $D(r)$ for graphene fragments of different sizes and shapes, gave the best agreement between the correlation functions of DC1000 and an isolated rectangular fragment with four hexagons on a side [11]. Two parallel fragments 3.35 Å apart, with the AB stacking analogous to that of bulk graphite, gave a very poor fit. Thus, we may conclude that both DC650 and DC1000 consist of small graphene fragments with lateral dimensions of the order of 10 Å. Intergraphene correlations are undetectable in $D(r)$, implying the absence of well defined interlayer C–C distances. The reasons for this could be a spread of interfragment separations, imperfect parallelism of adjacent fragments, and the lack of registry between them. A more detailed discussion of the structural analysis is given elsewhere [11].

2.2. Inelastic neutron scattering

We have confirmed that the disordered carbons investigated consist of hexagonal sp^2-hybridized carbon networks. Thus, the residual hydrogen is most probably bonded to edge atoms, passivating some fraction of the dangling bonds in analogy to the case for hydrogenated amorphous silicon. However, a variety of C–H bonding environments occur in different amorphous hydrocarbon materials, and a general tendency for H to saturate π-bonds, converting sp^2 to sp^3 carbon, was also observed [9]. In order to probe the local hydrogen environment at the edges of graphene fragments, we have performed inelastic neutron scattering (INS) experiments.

Inelastic neutron scattering is similar to Raman scattering (i.e., inelastic light scattering) in the sense that probing particles absorb or emit a quantum of energy in the sample (e.g., a quantum of vibrational energy, or phonon). However, vibrational spectroscopy based on INS offers several advantages over the more familiar Raman spectroscopy—in particular, very high sensitivity to modes involving hydrogen motion, and the absence of symmetry selection rules, such that all modes are in principle detectable. Hydrogen is a very strong incoherent scatterer, with an incoherent scattering cross-section $\sigma_{\mathrm{inc}}(\mathrm{H}) = 80.27$ b (1 barn $= 10^{-28}$ m^2) which is more than an order of magnitude larger than the total scattering cross-section of carbon. Whereas sophisticated procedures were necessary to remove the incoherent background in the RDF analysis, in inelastic scattering from hydrogen-rich materials all scattering can be assumed incoherent. The double-differential cross-section of a one-component system is then related directly to the density of vibrational states $G(\omega)$ [12]:

$$\left(\frac{\mathrm{d}^2\sigma}{\mathrm{d}\Omega\,\mathrm{d}E}\right)_{\mathrm{inc}} = \frac{k_f}{k_0}\frac{\sigma_{\mathrm{inc}}}{4\pi}S_{\mathrm{inc}}(\boldsymbol{Q},\omega) = \frac{k_f}{k_0}\frac{\sigma_{\mathrm{inc}}}{4\pi}\frac{3}{2M}\mathrm{e}^{-2W(\boldsymbol{Q})}\frac{\hbar\overline{|\boldsymbol{Q}\cdot\boldsymbol{e}|^2_\omega}}{E}\left\langle n+\frac{1}{2}\pm\frac{1}{2}\right\rangle G(\omega) \qquad (2)$$

where k_0, k_f are the incident and final neutron wave vectors, $Q = k_0 - k_f$ is the momentum transfer, M is the mass of hydrogen, $E = \hbar\omega$ is the energy transfer, and $\exp(-2W(\boldsymbol{Q})) = \exp(-Q^2\langle u^2\rangle/3)$ is the Debye–Waller factor ($\langle u^2\rangle$ denotes the mean square displacement). The expression $\overline{|\boldsymbol{Q}\cdot\boldsymbol{e}|^2_\omega}$ means the scalar product with the mode polarization vectors $\boldsymbol{e}_j$, averaged over all phonon modes j and phonon wave vectors at frequency ω. $\langle n\rangle$ is the temperature-dependent Bose occupation number of vibrational modes, $\langle n\rangle = 1/(\mathrm{e}^{E/k_BT} - 1)$, and the $\pm$ sign in equation (2) refers to phonon emission and absorption, respectively.

Two complementary techniques, filter–analyser neutron spectroscopy (FANS) and time-of-flight (TOF) spectroscopy, were employed in our inelastic scattering experiments. We used the FANS instrument at the NIST research reactor, with two filter–analyser options: a lower-resolution filter (a block of polycrystalline Be metal), having an effective analyser energy resolution 3.5 meV, and a combination filter (polycrystalline Be and polycrystalline graphite)

for which the resolution is ∼1.2 meV. A copper Cu(220) monochromator was used, limiting the neutron energy at the low end to ∼35 meV. In FANS experiments, the scattered intensity, measured for a fixed monitor count of incident neutrons, is directly proportional to $S(Q, \omega)$ or the density of states.

The inelastic scattering at lower energies was measured using the Fermi-chopper cold-neutron time-of-flight instrument, also at NIST. In this instrument, a set of monochromators selects the incident neutron wavelength 4.8 Å, and a rotating Fermi chopper with curved slots produces monochromatic pulses that hit the sample at precise time intervals. The scattered neutrons are detected by an array of detectors arranged at a fixed distance from the sample, and by measuring the flight time of the neutrons, their final energy can be determined. From the set of neutron counts in all detectors and for all time channels, the scattering function $S(Q, \omega)$ can be derived by a straightforward procedure. More details on both FANS and TOF methods are given elsewhere [13, 14].

FANS spectra of the disordered carbons DC650 and DC1000, measured at temperature

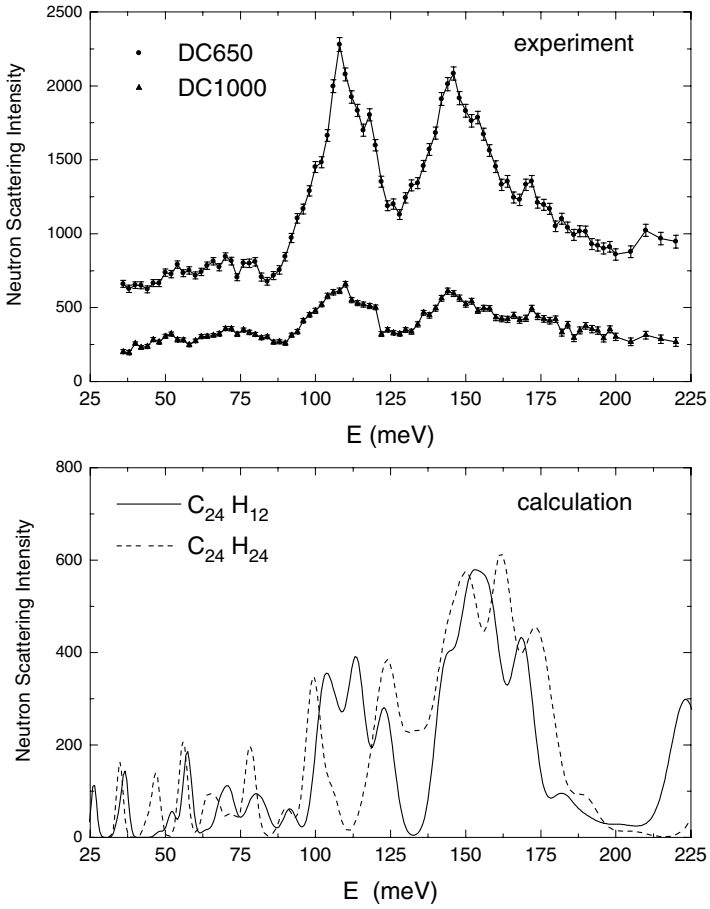

Figure 4. Top panel: inelastic neutron scattering spectra of the disordered carbons DC650 (circles, upper line) and DC1000 (triangles, bottom line) measured using FANS at 16 K. Bottom panel: the AM1 calculation of the inelastic scattering intensity for coronene, $C_{24}H_{12}$, and a similar molecule but with two H atoms per edge carbon, $C_{24}H_{24}$.

16 K, are shown in figure 4. The vibrational spectra of both display two prominent bands centred near 110 meV and 150 meV (in wavenumbers, commonly used in optical spectroscopies, 1 meV is equivalent to 8.066 cm^{-1}). The observed much smaller intensity of scattering from DC1000 is the consequence of its lower hydrogen content. Otherwise, the spectra of DC650 and DC1000 are quite similar, which suggests that the hydrogen configurations are the same in the two carbons. In aromatic molecules, vibrational modes above 95 meV correspond to C–H-bond out-of-plane bending vibrations, and modes in the range 140–180 meV correspond to C–H in-plane bending vibrations. Such an assignment is also supported by a theoretical calculation of the inelastic scattering intensity for coronene $C_{24}H_{12}$ (figure 4, lower panel). This calculation is based on mode frequencies and polarization vectors obtained by the quantum mechanical semiempirical MNDO/AM1 method [15], which was demonstrated to perform well for conjugated and aromatic systems. For comparison, a similar calculation was also performed for a coronene-shaped molecule but with two hydrogens per edge carbon, $C_{24}H_{24}$. The experimental results are clearly in better agreement with the former, providing strong evidence for the single H saturation per edge C atom.

Both broad features in figure 4 display a composite character and consist of several overlapping peaks. Higher-resolution spectra were obtained for the DC650 sample using the FANS Be/graphite filter, and are shown in figure 5, together with calculations for coronene, and a larger PAH molecule, ovalene $C_{32}H_{14}$. The splitting of the 110 meV band is well resolved in these data. As follows from the calculated spectra, the peaks in both bands are due to vibrational modes that have the same main character (i.e., out-of-plane or in-plane C–H bending) but differ in the relative phase with which the adjacent hydrogens move. We also notice that the calculated intensity of the band near 150 meV is larger than that observed

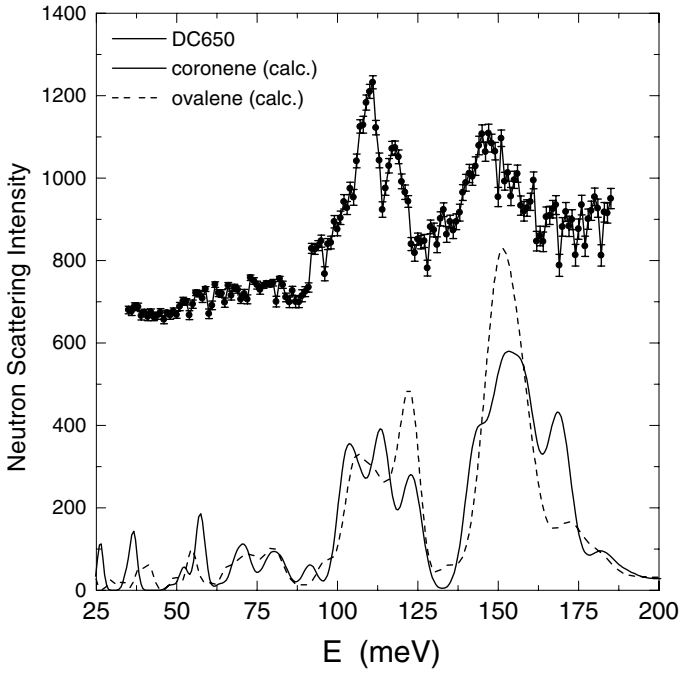

Figure 5. A FANS spectrum of the DC650 carbon, measured at 16 K using the higher-resolution Be/graphite filter. The solid and dashed lines below are results of AM1 calculations for coronene and ovalene ($C_{32}H_{14}$), respectively.

experimentally; this may be caused by a small underestimation of the Debye–Waller factor in the calculations.

Several smaller but well defined peaks below 90 meV are calculated for both coronene and ovalene. These peaks are due to vibrational modes that involve molecular skeleton deformations (mainly C–C–C-bond-angle bending and out-of-plane torsional vibrations). We indeed observe an increased scattering intensity in this energy range in the DC650 carbon, although no specific peaks could be resolved. This may be explained by a wide distribution of shapes and sizes of graphene fragments, each having slightly different frequencies of these skeleton modes, such that the scattering is effectively smeared out in this region.

The disordered carbon NT10 has the highest hydrogen content (H/C ratio 0.38), and thus is a strong incoherent scatterer. Its FANS spectra, measured at 16 K, are shown in figure 6. Also shown are the measured inelastic spectra of coronene and polyethylene, both in crystalline powder forms. The spectra were renormalized to approximately the same hydrogen content, and are offset vertically for clarity. The similarity between NT10 and coronene is quite striking, and implies that the graphene fragment sizes in NT10 are comparable to that of the coronene molecule, and have a similar edge topology. In contrast, the FANS spectra of polyethylene, $(–CH_2–)_n$, are very different, and display well defined peaks due to rocking, twisting, and wagging vibrations of the CH_2 groups. We can conclude that even at high hydrogen concentrations in this class of disordered carbons, the content of methylene groups in these materials is negligible.

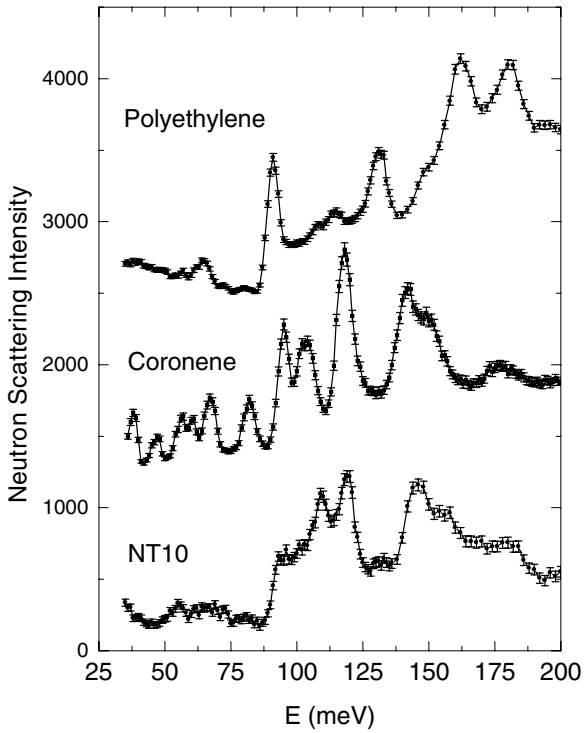

Figure 6. FANS spectra of the disordered carbon NT10, coronene, and polyethylene, measured at 16 K. The data were renormalized to the same hydrogen content, and are offset vertically for clarity.

Well defined peaks were resolved in the inelastic spectrum of coronene over the whole

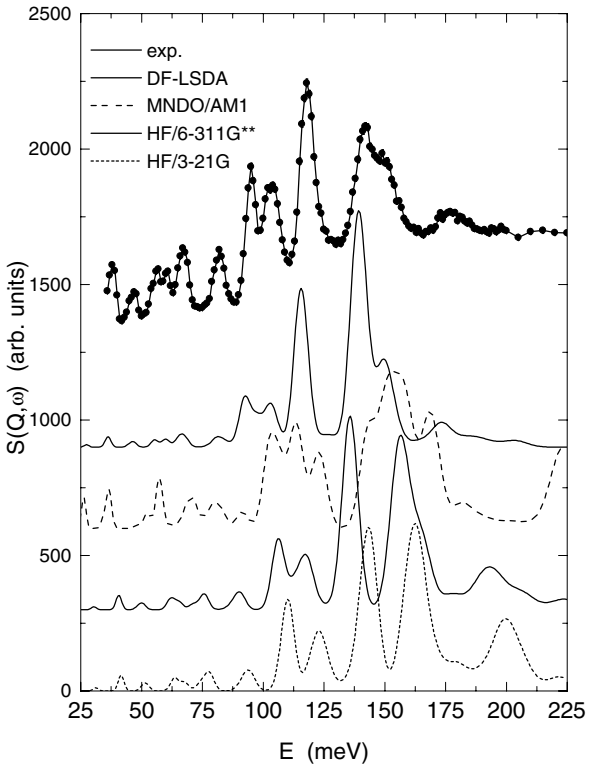

Figure 7. $S(Q, \omega)$ calculated for coronene, obtained by (from the bottom upwards) the Hartree–Fock method using the 3-21G basis, the Hartree–Fock method using the 6-311G** basis, the semiempirical AM1 method, and the density-functional LSDA method. Experimental FANS data are plotted for comparison.

energy range of the FANS measurements. It is quite instructive to compare these data with calculations at higher levels of theory. Figure 7 shows $S(Q, \omega)$ for coronene calculated by the density-functional method using the local spin-density approximation (LSDA) [16], the semiempirical AM1 method, and mean-field Hartree–Fock methods using a large atomic basis 6-311G** and a smaller basis set 3-21G [17]. The best agreement with experiment is achieved by the density-functional LSDA method; the calculated *unscaled* vibrational frequencies correspond to within a few per cent with measured values, and also agree well with scaled frequencies calculated by Martin [18]. Whereas the AM1 method performs reasonably well, the Hartree–Fock results are shifted significantly to higher values (for this reason, it is common to multiply calculated frequencies by an *ad hoc* scale factor <1). It is obvious that this shift also depends on the size of the atomic basis set and is smaller if a large basis set is used. The mean-field Hartree–Fock method, unlike density-functional theory, neglects electron correlations, which implies that correlation effects play an important role in determining the vibrational frequencies also for the C–H bending modes. The observed and calculated values are summarized in table 1, together with mode symmetries and brief descriptions. Modes observed in the time-of-flight experiments, as described below, are also included in the table.

We should point out that many of the observed modes possess such symmetries that they are neither IR nor Raman active. For example, the intense peak at 118 meV has the a_{1u} symmetry, and is not readily identified by optical spectroscopic methods. However, since this

Table 1. A summary of the vibrational modes of coronene observed by means of inelastic neutron scattering, the frequencies calculated using the density-functional LSDA, the B3LYP functional (after reference [18]), and the Hartree–Fock/6-311G** and AM1 methods, and the symmetries and descriptions of the modes. Frequencies are listed in meV units; 1 meV = 8.066 cm^{-1}. Abbreviations: o.o.p. denotes out-of-plane and i.p. in-plane modes.

INS	LSDA	B3LYP	HF/6-311G**	AM1	Symmetry	Description
2.8	—	—	—	—	—	3D acoustic phonon
5.0	—	—	—	—	—	3D acoustic phonon
14.5	15.3	15.8	17.0	16.0	a_{2u}	o.o.p. carbon torsions
18.7, 22.5	20.1	20.0	22.4	18.0	b_{1g}	o.o.p. carbon torsions ($q = \pi$ and $q = 0$ optical phonons)
28.5	27.4	27.6	30.4	26.1	b_{2g}	o.o.p. carbon torsions
37.0	36.6	36.8	40.7	34.5	e_{2u}	o.o.p. carbon torsions
46.0	45.1	44.7	48.7	48.1	e_{2g}	i.p. C–C–C bend
57.0	55.3	55.6	61.6	51.7	e_{1g}	o.o.p. carbon torsions
60.0	59.9	60.0	65.5	67.3	e_{2g}	i.p. C–C–C bend
67.0	67.9	70.3	75.9	71.4	a_{2u}	o.o.p. carbon torsions + o.o.p. C–H bend
82.0	80.8	83.6	90.9	82.2	e_{1g}	o.o.p. carbon torsions + o.o.p. C–H bend
95.0	93.0	94.4	106.3	102.7	b_{1g}	o.o.p. C–H bend
103.0	105.0	107.2	119.4	114.2	a_{2u}	o.o.p. C–H bend
118.0	114.2	116.8	134.3	120.6	a_{1u}	o.o.p. C–H bend
142.0	139.1	138.7	157.7	143.1	b_{2u}	i.p. C–H bend
149.0	149.6	149.9	167.0	157.2	a_{2g}	i.p. C–H bend
177.0	172.1	172.3	193.0	180.8	b_{1u}	i.p. C–H bend

mode involves significant hydrogen motions (C–H out-of-plane bending, with neighbouring H atoms moving in opposite phases), it produces a strong peak in the inelastic neutron spectra. Thus, our data essentially complete the available experimental information on the vibrational dynamics of coronene.

In figure 8 we present the time-of-flight results for the disordered carbons DC650 and DC1000, and for coronene, measured at 250 K. The TOF spectra are for both disordered carbons featureless, except for a single broad peak positioned at ∼1.7 meV for both samples. Such a feature is well known from inelastic neutron and low-frequency Raman spectra of amorphous materials below the glass transition, and is called the boson peak [19, 20]. The precise origin of this peak is not well understood, and it has been attributed to localization of vibrational modes caused by the disorder in glassy materials [21]. Molecular dynamics simulations for polymer glasses suggest that this feature is due to collective dynamics determined mainly by intermolecular interactions [22]. The observation of the boson peak at the same position for DC650 and DC1000 is quite interesting, and implies that despite a considerably different hydrogen content in these samples, their dynamics are very similar even at the very low frequencies.

In the TOF spectrum of coronene (figure 8, lower panel), several well defined peaks can be observed. We assign the double peak at 2.8 meV and 5 meV to acoustic phonon modes in crystalline coronene. The smaller peaks at 14.5, 18.7, 22.5, and 28.5 meV are due to weakly dispersed low-frequency optical modes that involve torsions of the dihedral angles of the molecular framework. The fact that no similar peaks are found in this frequency range for disordered carbons once again confirms that there is no preference for a particular shape of the graphene fragments.

Inelastic scattering spectra of the successfully Li-doped DC650 carbon were measured using both the FANS and TOF techniques, and are shown in figure 9. The TOF data display

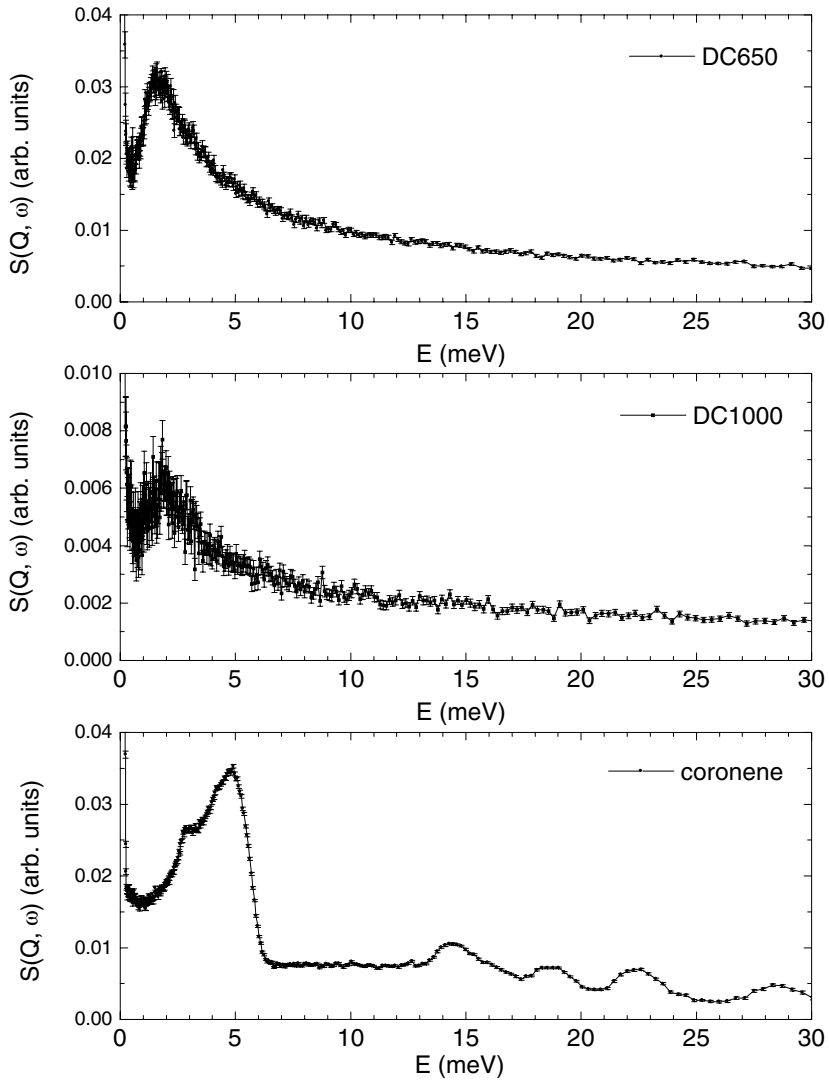

Figure 8. Time-of-flight inelastic scattering results for the disordered carbons DC650 (upper panel) and DC1000 (middle panel), and crystalline coronene (lower panel), measured at 250 K.

an apparent shift in the position of the boson peak (from 1.7 to 2.3 meV) upon doping. The intensity of this peak is also much smaller for the Li-doped carbon (this effect is not due to neutron absorption by the ^{6}Li isotope (natural abundance 7.5%) which has been taken into account in the data treatment). While we do not have a definite explanation for this observation, the shift implies that the low-frequency dynamics is affected by the introduction of lithium in the system. The lithium and graphene fragments interact in disordered carbons, contrary to suggestions that the Li capacity of these materials is determined by the morphology and specific surface area rather than the microstructure, and lithium is simply accumulated in inter-particle voids [23]. The Li atoms must penetrate the disordered carbon particles for the shift to occur.

The effects of Li doping are more subtle in FANS spectra (figure 9(b)). Here we observe

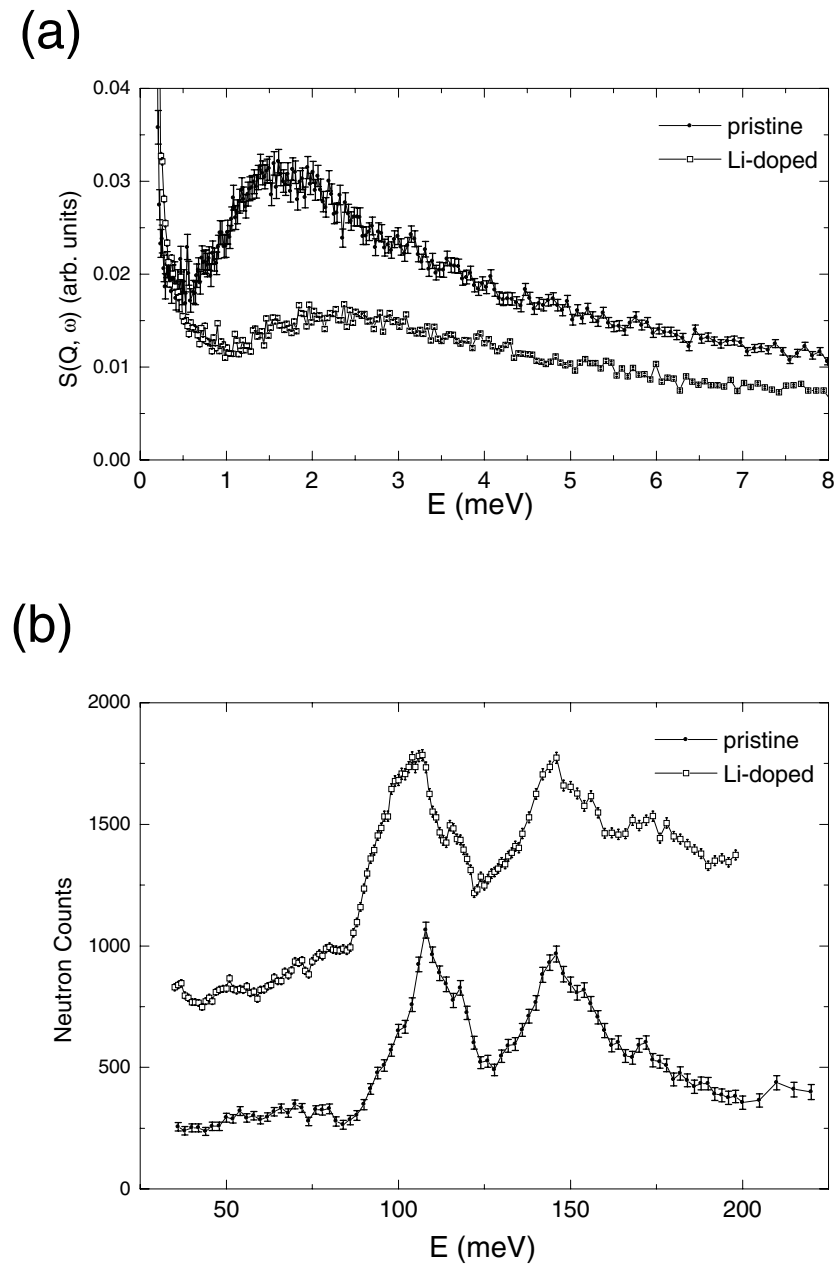

Figure 9. (a) Comparison of time-of-flight results for pristine DC650 (solid dots, upper line), and lithium-doped DC650 (open squares, bottom line), measured at 250 K. The data are offset vertically by 0.005 for clarity. (b) Comparison of FANS spectra of pristine and Li-doped disordered carbon DC650 (solid dots and open squares, respectively), measured at 16 K. The spectra are offset vertically for clarity.

a small (∼2–3 meV) downshift, and broadening of the first strong band due to C–H bond out-of-plane bending vibrations. A similar effect is found in the doped conjugated polymer polyacetylene, where a downshift of the C–H bending modes occurs due to charge transfer

between dopants and polymer chains. However, preliminary calculations for charged PAH molecules suggest that a complete charge transfer would have a much more pronounced effect on these modes than is observed. Partial charge transfer and/or formation of C–Li bonds can be reconciled more easily with the experimental data. Additional experimental and theoretical work is necessary to characterize the vibrational dynamics in doped disordered carbons.

3. Conclusions

In this paper, we have presented the results from a variety of neutron scattering techniques employed to study the composition, local structure, and vibrational dynamics of several disordered carbon anode materials. The principal findings can be summarized as the following points:

(1) As expected, the materials synthesized by pyrolysis of organic precursors at relatively low temperatures consist of graphene fragments (i.e., sp^2-hybridized carbon in a hexagonal network), and retain substantial residual hydrogen.
(2) There is a negligible amount of methylene (CH_2) and other functional (H-containing) groups, implying one terminal hydrogen per edge C atom; this is a necessary condition for a second lithium uptake mechanism involving the formation of polar C–Li bonds at the edges.
(3) The lack of well defined low-frequency modes suggests a wide variety of shapes and sizes of graphene fragments. Thus, the disordered carbons can be viewed as a distribution of large polycyclic aromatic hydrocarbons. A boson peak is observed, characteristic for glassy or disordered materials, and its position is independent of the hydrogen content in the material.
(4) Upon lithium doping, effects are observed that are consistent with partial charge transfer from Li to the carbons as well as C–Li bonding. A shift of the boson peak is also observed, although the nature of this phenomenon is not yet understood. Additional experimental work is necessary to characterize the doped systems.

Acknowledgments

We would like to thank Rick Paul for his assistance with the PGAA analysis, and T Zheng and J R Dahn who graciously provided the carbon samples. This work was funded in part by the Department of Energy under contract DEFC02-86ER45254. The use of supercomputing facilities at NIST and at the National Energy Research Scientific Computing Center is also acknowledged.

References

[1] Dahn J R, Zheng T, Liu Y and Xue J S 1995 *Science* **270** 590
[2] Fischer J E 1987 *Chemical Physics of Intercalation* ed A P Legrand and S Flandrois (New York: Plenum) p 59
[3] Sato K, Noguchi M, Demachi A, Oki N and Endo M 1994 *Science* **264** 556
[4] Avdeev V V, Nalimova V A and Semenenko K N 1990 *High Pressure Res.* **6** 11
[5] Papanek P, Radosavljevic M and Fischer J E 1996 *Chem. Mater.* **8** 1519
[6] Nakadaira M, Saito R, Kimura T, Dresselhaus G and Dresselhaus M S 1997 *J. Mater. Res.* **12** 1367
[7] Heiney P A, Huster M E, Cajipe V B and Fischer J E 1985 *Synth. Met.* **12** 21
[8] Petkov V, DiFrancesco R G, Billinge S J L, Acharya M and Foley H C 1999 *Phil. Mag.* B **79** 1519
[9] Walters J K and Newport R J 1995 *J. Phys.: Condens. Matter* **7** 1755
[10] Crawford R K, Price D L, Haumann J R, Kleb R, Montague D G, Carpenter J M, Susman S and Dejus R J 1989 *Proc. 10th Mtg on Advanced Neutron Sources* vol 97 (Bristol, UK: Institute of Physics Publishing) p 419

[11] Zhou P, Papanek P, Lee R, Fischer J E and Kamitakahara W A 1997 *J. Electrochem. Soc.* **144** 1744
[12] Price D L and Sköld K 1986 Introduction to neutron scattering *Methods of Experimental Physics: Neutron Scattering* vol 23, ed K Sköld and D L Price (Orlando, FL: Academic) p 1
[13] Papanek P, Fischer J E, Sauvajol J L, Dianoux A J, Mao G, Winokur M J and Karasz F E 1994 *Phys. Rev.* B **50** 15 668
[14] Copley J R D and Udovic T J 1993 *J. Res. Natl Inst. Stand. Technol.* **98** 71
[15] Dewar M J S, Zoebish E G, Healy E F and Stewart J J P 1985 *J. Am. Chem. Soc.* **107** 3902
[16] In this calculation, we used Slater exchange:
Slater J C 1974 *Quantum Theory of Molecules and Solids* vol 4 (New York: McGraw-Hill)
and Vosko–Wilk–Nusair correlation functionals:
Vosko S H, Wilk L and Nusair M 1980 *Can. J. Phys.* **58** 1200
and an atomic basis set of the same quality as in the HF/6-311G** calculation.
[17] Frisch M J *et al* 1995 *Gaussian 94* Revision B.1, Gaussian Incorporated, Pittsburgh, PA
[18] Martin J M L 1996 *Chem. Phys. Lett.* **262** 97
[19] Frick B and Richter D 1995 *Science* **267** 1939
[20] Annis B K, Lohse D J and Trouw F 1999 *J. Chem. Phys.* **111** 1699
[21] Wischnewski A, Buchenau U, Dianoux A J, Kamitakahara W A and Zarestky J L 1998 *Phil. Mag.* B **77** 579
[22] Ahlström P, Wahnström G, Carlsson P, Schantz S, Brodin A, Maurer F and Torell L 1998 *Phil. Mag.* B **77** 699
[23] Disma F, Aymard L, Dupont L and Tarascon J M 1996 *J. Electrochem. Soc.* **143** 3959